



Detection of Linear Polarization in the Radio Remnant of Supernova 1987A

Giovanna Zanardo¹, Lister Staveley-Smith¹, B. M. Gaensler², Remy Indebetouw^{3,4},
C.-Y. Ng⁵, Mikako Matsuura^{6,7}, and A. K. Tzioumis⁸

¹International Centre for Radio Astronomy Research, M468, University of Western Australia, Crawley, WA 6009, Australia; giovanna.zanardo@gmail.com

²Dunlap Institute for Astronomy & Astrophysics, University of Toronto, Toronto, ON M5S 3H4, Canada

³Department of Astronomy, University of Virginia, P.O. Box 400325, Charlottesville, VA 22904-4325, USA

⁴National Radio Astronomy Observatory, 520 Edgemont Road, Charlottesville, VA 22903, USA

⁵Department of Physics, University of Hong Kong, Pokfulam Road, Hong Kong

⁶Department of Physics and Astronomy, University College London, Gower Street, London WC1E 6BT, UK

⁷School of Physics and Astronomy, Cardiff University, Queens Buildings, The Parade, Cardiff, CF24 3AA, UK

⁸CSIRO Astronomy and Space Science, Australia Telescope National Facility, PO Box 76, Epping, NSW 1710, Australia

Received 2018 May 15; revised 2018 June 12; accepted 2018 June 12; published 2018 June 29

Abstract

Supernova (SN) 1987A in the Large Magellanic Cloud (LMC) has proven to be a unique laboratory within which to investigate particle acceleration in young supernova remnants (SNRs). Here we report the first detection of linear polarization of the supernova's synchrotron emission from imaging observations at frequencies spanning from 20 to 50 GHz, carried out with the Australia Telescope Compact Array (ATCA) between 2015 October and 2016 May. The direction of the radio polarization, corrected for Faraday rotation, points to a primarily radial magnetic field across the inner ring, encompassing both the reverse and forward shocks. The magnetic field strength peaks over the high-emissivity eastern sites, where efficient cosmic-ray acceleration likely takes place under quasi-parallel shocks at high Mach numbers. The mean fraction of polarized emission in the brightest sites is $2.7\% \pm 0.2\%$ at 22 GHz and $3.5\% \pm 0.7\%$ at 44 GHz. In the inner remnant, non-radial components of the polarized emission appear to be more prevalent. However, the low significance detection in the central regions limits interpretation.

Key words: acceleration of particles – cosmic rays – ISM: magnetic fields – ISM: supernova remnants – polarization – supernovae: individual (SN 1987A)

1. Introduction

Supernova remnants (SNRs) are powerful particle accelerators. As a supernova (SN) blast wave propagates through the circumstellar medium (CSM), electrons and protons trapped between upstream and downstream magnetic mirrors gain energy via multiple traversals of the shock front (Drury 1983; Kirk et al. 1996). The accelerated particles generate further magnetic field fluctuations and local amplification (Bell 2004), thus leading to increased acceleration efficiency (Koyama et al. 1995; Abdo et al. 2010; Ackermann et al. 2013). The geometry and orientation of the magnetic field that drive an efficient particle acceleration process by the shock front remain a subject of debate.

Although older SNRs have been observed with a preferentially tangential magnetic field, many young SNRs exhibit some degree of radial alignment (Reynolds & Gilmore 1993; Reynolds et al. 2012). Theoretical models show that the magnetic field lines can be stretched radially by the Rayleigh–Taylor (R–T) instability (Gull 1973) at the contact discontinuity between the SN ejecta and the compressed CSM. However, it is still unclear whether the R–T instability or another mechanism can reproduce a radial field that extends outward to the forward shock (Badjin et al. 2016). According to ideal magneto-hydrodynamics (MHD), a radial field that reaches the forward shock can be obtained when cosmic rays significantly contribute to the shock pressure (Schure et al. 2009), a scenario that implies fast shocks with efficient particle acceleration (Blondin & Ellison 2001). The diffusion of cosmic rays in SNRs depends on the field orientation and the level of magnetic turbulence which, in turn, can result from the

instability induced by the cosmic-ray pressure gradient (Drury & Downes 2012). MHD simulations suggest that turbulent fields driven by hydrodynamic instabilities (Inoue et al. 2013; Bandiera & Petruk 2016) may have radially biased velocity dispersions, leading to selective amplification of the radial component and further cosmic-ray production.

The remnant of SN 1987A in the Large Magellanic Cloud (LMC) has proven to be a unique laboratory for investigating particle acceleration in young SNRs (Petruk et al. 2017; Zanardo et al. 2017). At the current stage of the evolution of the radio remnant, the synchrotron emission observable at radio frequencies mostly originates from the shock wave interacting with high-density CSM in the equatorial plane (e.g., Zanardo et al. 2013, 2014, and references therein), distributed in a ring-like structure (equatorial ring (ER)). The emission around the ER can be fitted in the Fourier space via a thick torus (Ng et al. 2008, 2013), although the shocks are now expanding above and below the equatorial plane and interacting with high-latitude material confined within the nebula hourglass structure (Potter et al. 2014).

This Letter presents the results of polarimetric observations of SNR 1987A carried out with the Australia Telescope Compact Array (ATCA) between 2015 October and 2016 May, from 20 to 50 GHz. Details of the observations and data reduction are given in Section 2. In Section 3, we describe the extraction of the polarization components and introduce ad hoc polarization parameters. The implications of the detection of polarized emission for the magnetic field in the SNR and, thus, particle acceleration and cosmic-ray production by the shock front, are discussed in Section 4.

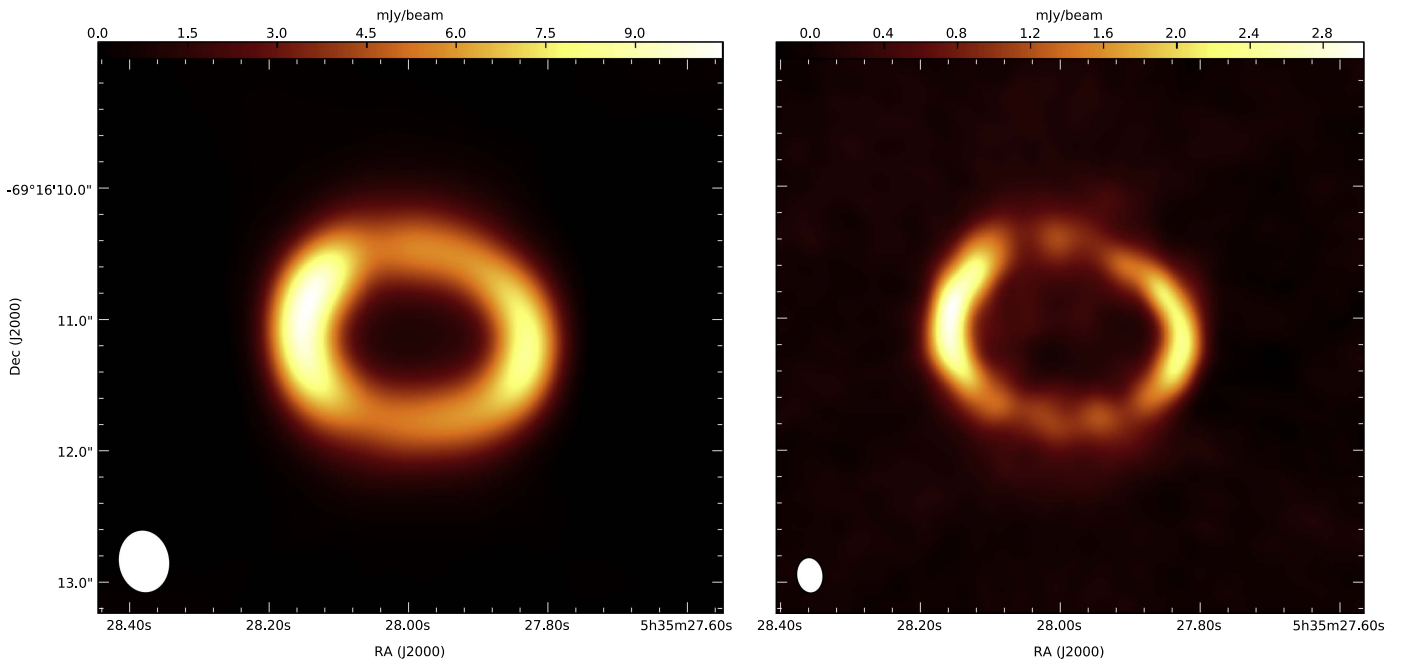


Figure 1. Diffraction-limited Stokes- I continuum images of SNR 1987A at 22 GHz (left) and 44 GHz (right) obtained from ATCA observations carried out from 2015 October to 2016 May. The beam size (FWHM) is $0''.48 \times 0''.39$ at 22 GHz and $0''.27 \times 0''.20$ at 44 GHz, as plotted in the lower-left corner of each image.

2. Observations

SNR 1987A was observed at 7 and 15 mm wavelengths (λ) with the ATCA in 2015 October 16–19 and 2016 May 17–18, with 2×12 hr sessions on each frequency band in 2015 October and one 12 hr session on each band in 2016 May. In all sessions the ATCA was in the 6A configuration with a maximum baseline of 5939 m. The observations were performed over 2×2 GHz bandwidth in each frequency band, centered on 22.2 and 23.7 GHz, and 43.4 and 49.0 GHz, respectively. Atmospheric conditions were optimal during all October sessions with the rms of the path length fluctuations below $300 \mu\text{m}$. In all observations, the standard bandpass calibrator PKS B0637–752 was observed for 2 minutes every 90 minutes, while the phase calibrator PKS 0530–727 was observed for 1.5 minutes every 6 minutes on the source. Uranus was used as the flux density calibrator at 43.4 and 49.0 GHz. At 22.2 and 23.7 GHz, we used PKS B1934–638 as the primary flux density calibrator. The data were reduced with MIRIAD.⁹ Polarization leakage corrections were applied via the task `gpcal`, based on the polarization properties of the calibrator. To avoid bandwidth depolarization, the data were reduced separately for 400 MHz sub-bands. A weighting parameter (Briggs 1995) of `robust = 0.5` was used in all bands for Stokes- I images, and `robust = 2.0` was used for the derivation of Stokes- Q , $-U$, and $-V$ images. For Stokes- I data, deconvolution was carried out via the maximum entropy method (Gull & Daniell 1978), while no further deconvolution was performed on the Stokes- Q , $-U$, and $-V$ maps. The integrated flux density of the Stokes- I images is ~ 92 mJy at 22 GHz and ~ 59 mJy at 44 GHz. The angular resolution, defined as the FWHM of the approximately Gaussian central lobe of the restoring beam, is $0''.4$ for the 22 GHz image and $0''.2$ for the 44 GHz map (Figure 1).

⁹ <http://www.atnf.csiro.au/computing/software/miriad/>

3. Polarization Measurements

3.1. Rotation Measure (RM)

For linearly polarized radio emission at short wavelengths or Faraday-thin objects (Sokoloff et al. 1998), the observed polarization angle ψ is linked to the Faraday RM as (Burn 1966)

$$\psi = \psi_0 + \text{RM} \lambda^2, \quad (1)$$

with ψ_0 the intrinsic polarization angle. For wavelengths so close that $|\lambda_{i+1}^2 - \lambda_i^2| < \pi/2 \text{RM}_0$ (Ruzmaikin & Sokoloff 1979), the general definition of $\text{RM} \approx d\psi(\lambda)/d\lambda^2$ can be taken as a linear function of λ^2 , i.e., $\text{RM}_{i+1,i} \approx (\psi_{i+1} - \psi_i)/(\lambda_{i+1}^2 - \lambda_i^2)$, being $\lambda_{i+1} > \lambda_i$.

In our analysis, λ_i and λ_{i+1} are taken as the central wavelengths of adjacent 400 MHz wide frequency sub-bands, i.e., $\lambda_i = \lambda_0 + i \Delta\lambda$, and $i = 0, 1 - 3$ within each 2 GHz bandwidth (see Section 2). Due to high ψ uncertainty associated with the fainter polarized emission at higher frequencies, the RM could not be estimated for sub-bands in the ~ 48.5 – 50.0 GHz frequency range (Figure 2).

3.2. Linear Polarization Components

The linear polarized intensity, $I_p = \sqrt{Q^2 + U^2}$, is the modulus of the Q and U Stokes parameters. The I_p distribution across SNR 1987A as observed at 22 GHz is shown in Figure 3, blanked for polarized emission intensity lower than 2σ . We note that bias in the observed linear polarization arises when the measurement of Q and U is significantly affected by noise, as the quantity $Q^2 + U^2$ is overestimated (Simmons & Stewart 1985). Assuming that the errors on the actual Stokes parameters, Q_0 and U_0 , are known and both equal to σ , i.e., $Q = Q_0 \pm \sigma$ and $U = U_0 \pm \sigma$, the true degree of polarization can be taken as (Simmons & Stewart 1985) $I_{p0} = \sqrt{Q_0^2 + U_0^2}$ if $I_{p0}/\sigma > 4$, with polarization angle $\psi_0 = 1/2 \tan^{-1} Q_0/U_0$. In

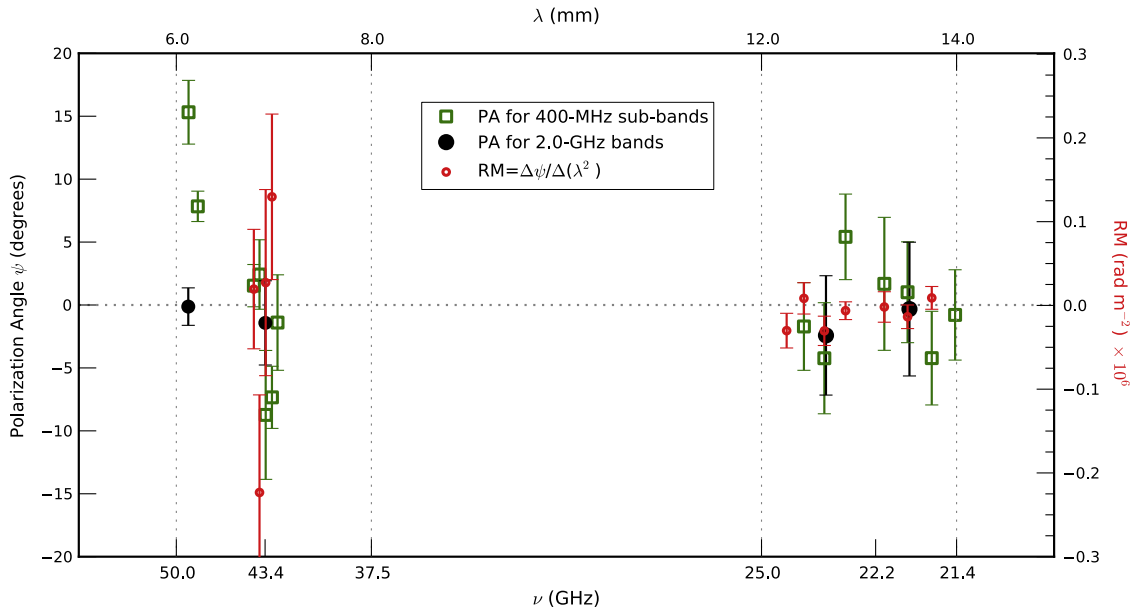


Figure 2. Polarization angle (ψ) and rotation measure (RM) vs. frequency. The wavelength dependence of ψ , being $\tan(2\psi) = U/Q$, and of RM, given $RM = \Delta\psi/\Delta(\lambda^2)$, is investigated for all observations of polarized emission from 20 to 50 GHz, from 2015 October to 2016 May, with reference to the compact brightest region on the eastern lobe (see Figure 1).

the case of our 3σ polarization measurements, I_p is over-estimated by $\sim 2\%$ at 22 GHz with an error on ψ_0 of less than 5° over the ring-like structure of the SNR, while at 44 GHz $(I_p - I_{p0})/I_{p0} \approx 3\%$ and $\psi = \psi_0 \pm 7^\circ$ over the brightest Stokes- I sites.

Similarly, the standard expression of the fractional polarization as a function of the Stokes parameters, $P \equiv \sqrt{Q^2 + U^2}/I$, is greatly affected by bias when the signal-to-noise ratio is low. To bypass this bias, we introduce two polarization parameters, quasi- E (or \hat{E}) and quasi- B (or \hat{B}) polarizations, which can be derived for emission distributions characterized by polar axis symmetry. These quasi-polarizations are obtained via polar transformation of the linear polarization Stokes parameters, Q and U , i.e.,

$$\begin{cases} \hat{E} = U \sin(2\chi) + Q \cos(2\chi) \\ \hat{B} = U \cos(2\chi) - Q \sin(2\chi), \end{cases} \quad (2)$$

where χ is the position angle of the Q and U measurements relative to the central reference. For radio sources with polar morphology such as SNRs, the \hat{E} and \hat{B} parameters are the orthogonal components of the electric field. In the specific case of SNR 1987A, the central reference is taken as the SN site (Reynolds et al. 1995), and the position angle χ is measured from north to east (see Figure 4). After correction for Faraday rotation, the \hat{E} and \hat{B} quantities trace the components of the magnetic field, aligned at $[0^\circ, 90^\circ]$ and $[-45^\circ, +45^\circ]$ to the tangent of the ring-like structure of the SNR, analogous to the E and B polarization modes (Zaldarriaga & Seljak 1997). As for the E sign convention, negative values of \hat{E} identify a radial pattern of the magnetic field, which we signify as \mathbf{B}_\parallel . Fitting of the \hat{E} versus I distribution allows a robust estimate of the fractional polarization in regions of varying brightness and, especially, in low-emissivity sites.

4. Discussion

As can be seen in the Stokes- I flux density distribution at mm $\lambda\lambda$ (Figure 1), the radio emission from the remnant of SNR 1987A currently extends beyond the ER, with linearly polarized emission in both the inner region of the SNR and over the ER (Figure 3). The derivation of \hat{E} and \hat{B} via Equation (2) (Figure 4) allows us to map the marked radial component of the magnetic field (\mathbf{B}_\parallel), which appears especially strong over the brightest regions on the eastern lobe (see \hat{E} map in Figure 4). The radial alignment is observed to be maintained through the ER, thus encompassing both the reverse and forward shocks, i.e., where the majority of the synchrotron emitting electrons is generated (Potter et al. 2014). While a predominantly radial magnetic field has been found in many young SNRs (Milne 1987), SNR 1987A is by far the youngest remnant to exhibit such alignment. Weaker non-radial field components appear localized in the NE sector just outside of the brightest regions of the remnant, as well as in the faintest Stokes- I sites on the ring, i.e., at position angle PA $\sim 225^\circ$ and PA $\sim 325^\circ$ (Figure 4).

Because the synchrotron brightness directly tracks the magnetic field strength, the association of the strongest \mathbf{B}_\parallel field with the high-emissivity sites on the eastern lobe of the SNR is consistent with the scenario of large injection efficiency and amplification of the magnetic field due to cosmic-ray production. The expansion velocity extrapolated for the faster eastbound shocks (Zanardo et al. 2013), $u \sim 6000 \text{ km s}^{-1}$, would yield high upstream Alfvénic Mach numbers, M_A , depending on the shock arrangement, being $M_A = u/v_A$ with $v_A \ll u$ the speed of the Alfvén waves generated by the cosmic rays. The detection in Saturn’s strong bow shock of electron acceleration under quasi-parallel magnetic conditions (Masters et al. 2013) suggests that when $M_A \sim 100$ quasi-parallel shocks become very effective electron accelerators. Globally high Mach numbers linked to quasi-parallel shocks likely result from nonlinear amplification of the magnetic field due to very efficient cosmic-ray acceleration (Bell & Lucek 2001), being

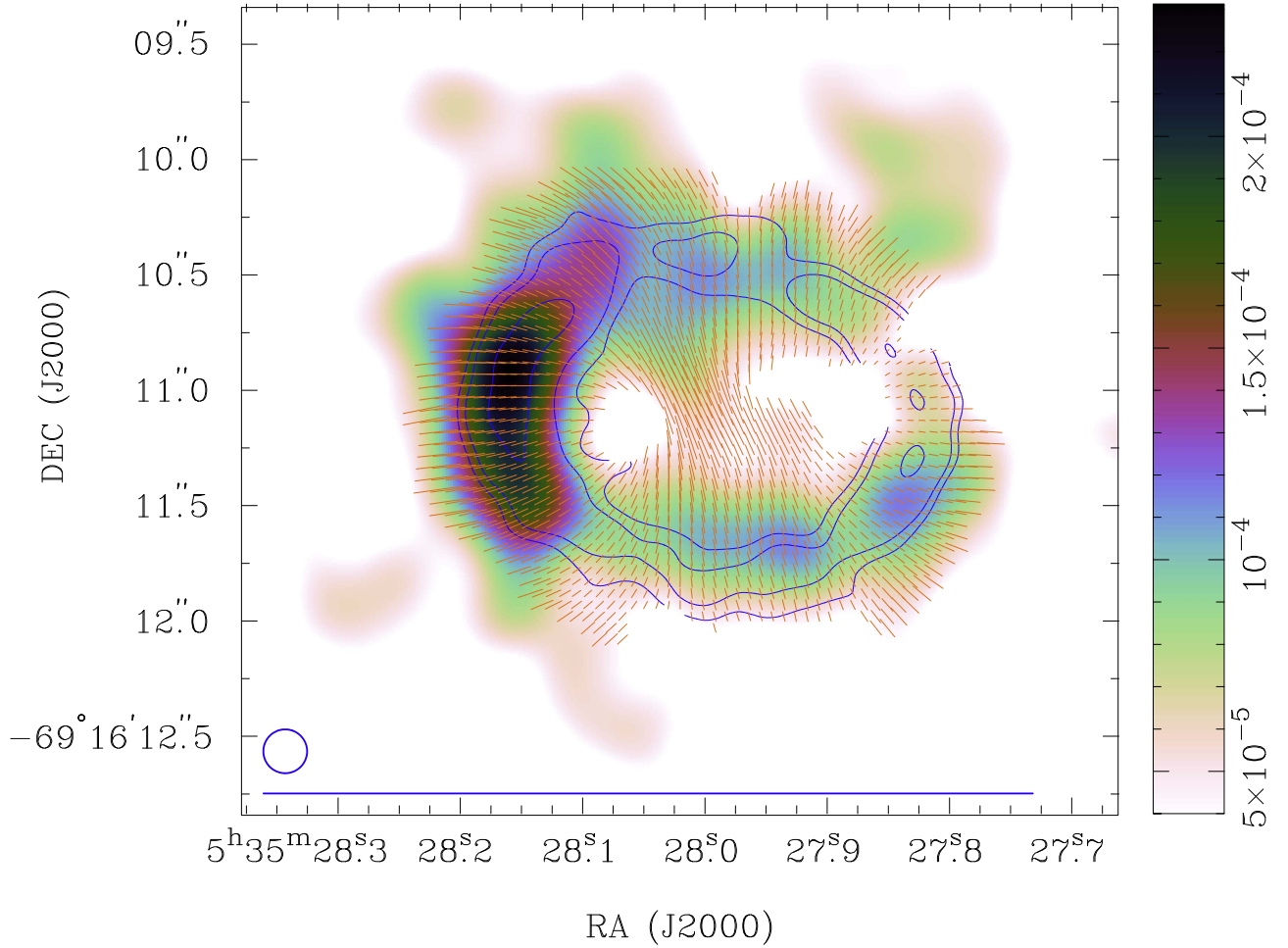


Figure 3. Map of the polarized intensity, defined as $I_p = \sqrt{Q^2 + U^2}$, where Q and U are the linear polarization Stokes parameters, generated for observations of SNR 1987A at 22 GHz. The map has an angular resolution (FWHM) of $0''.4$ and is shown with color scale in Jy beam^{-1} . The map is overlaid with the contours (blue) of the contemporaneous Stokes- I image of the SNR at 44 GHz, restored with a $0''.2$ circular beam (bottom-left corner). The 44 GHz contours are shown at flux density levels of 0.4, 6.0, and $1.5 \text{ mJy beam}^{-1}$. The polarization vectors have been rotated by 90° to show the intrinsic magnetic field orientation (orange lines). Vectors in the central region of the remnant are detections between $2\sigma_p$ and $3\sigma_p$, where $\sigma_p = 22.3 \mu\text{Jy beam}^{-1}$ the mean standard deviation of the noise in the Stokes- Q and $-U$ images. The vector length is proportional to the fractional polarization $P \equiv \sqrt{Q^2 + U^2}/I$; the line extent corresponding to $P = 100\%$ is shown at the bottom.

$M_A \propto (B_{\text{SNR}}/B_0)^2$, where B_{SNR} is the magnetic field strength within the SNR and B_0 is the magnetic field near the remnant.

The magnetic field strength within the SNR can be inferred from the energy equipartition and pressure equilibrium between the remnant magnetic field and cosmic rays (Beck & Krause 2005; Arbutina et al. 2012), which is

$$B_{\text{SNR}} \approx \left[G_0 G(\mathcal{K} + 1) \frac{S_\nu}{fd \theta_{\text{SNR}}^3} \nu^{\frac{(1-\gamma)}{2}} \right]^{\frac{2}{(5+\gamma)}}, \quad (3)$$

where G_0 is a constant, $G = G(\nu, \gamma)$ is the product of different functions varying with the minimum and maximum frequencies associated with the spectral component and the synchrotron spectral index (Beck & Krause 2005), \mathcal{K} is the ion/electron energy ratio, f is the volume filling factor of radio emission, $\theta_{\text{SNR}} = R_{\text{SNR}}/d$ is the angular radius, and $\gamma = 1 - 2\alpha$ with α the synchrotron spectral index, being the synchrotron emission $S_\nu \propto \nu^\alpha$. Considering that $1''.0 \lesssim R_{\text{SNR}} \lesssim 1''.1$, $-0.95 \leq \alpha \leq -0.91$, $20 \leq \nu \leq 50 \text{ GHz}$, $S_\nu = 92 \text{ mJy}$ at $\nu = 22 \text{ GHz}$, and taking $\mathcal{K} \approx 100$ while $f \approx 0.5$, Equation (3) yields $B_{\text{SNR}} \sim 2 \text{ mG}$. We note that although the equipartition of the magnetic field is a conjecture for young SNRs, it is considered

applicable (Sokoloff et al. 1998; Arbutina et al. 2012) for remnants or specific SNR sites where $-1.0 \lesssim \alpha \lesssim -0.8$, or for energy spectral indices $2 < \gamma \lesssim 3$. These conditions are met in the brightest eastern sites of SNR 1987A, i.e., in the regions that have been consistently associated with steeper synchrotron spectral indices (Zanardo et al. 2013, 2014).

We determine the strength of the ambient magnetic field, B_0 , i.e., the magnetic field within the CSM near the SN, from the RM (Figure 2). The magnetic field along the line of sight (LOS) can be linked to the RM as

$$\text{RM} \approx \frac{e^3 \lambda^2}{2\pi(m_e c^2)^2} \int_{\text{los}} n_e(l) B_{\text{los}}(l) dl. \quad (4)$$

Given $\text{RM} \approx 1.3 \times 10^5 \text{ rad m}^{-2}$, as the upper limit at $\sim 7 \text{ mm}$ wavelength (see Figure 2), and considering that the medium in which the SN radio emission propagates has an electron density $n_e \sim 110 \text{ cm}^{-3}$, as from low-frequency measurements by Callingham et al. (2016), Equation (4) yields $B_{\text{los}} \simeq B_0 \approx 28 \mu\text{G}$.

In this context, a nonlinear magnetic field amplification, $(B_{\text{SNR}}/B_0)^\theta$ with $1 < \theta \leq 2$, would lead to $100 \lesssim M_A \lesssim 10^3$. For

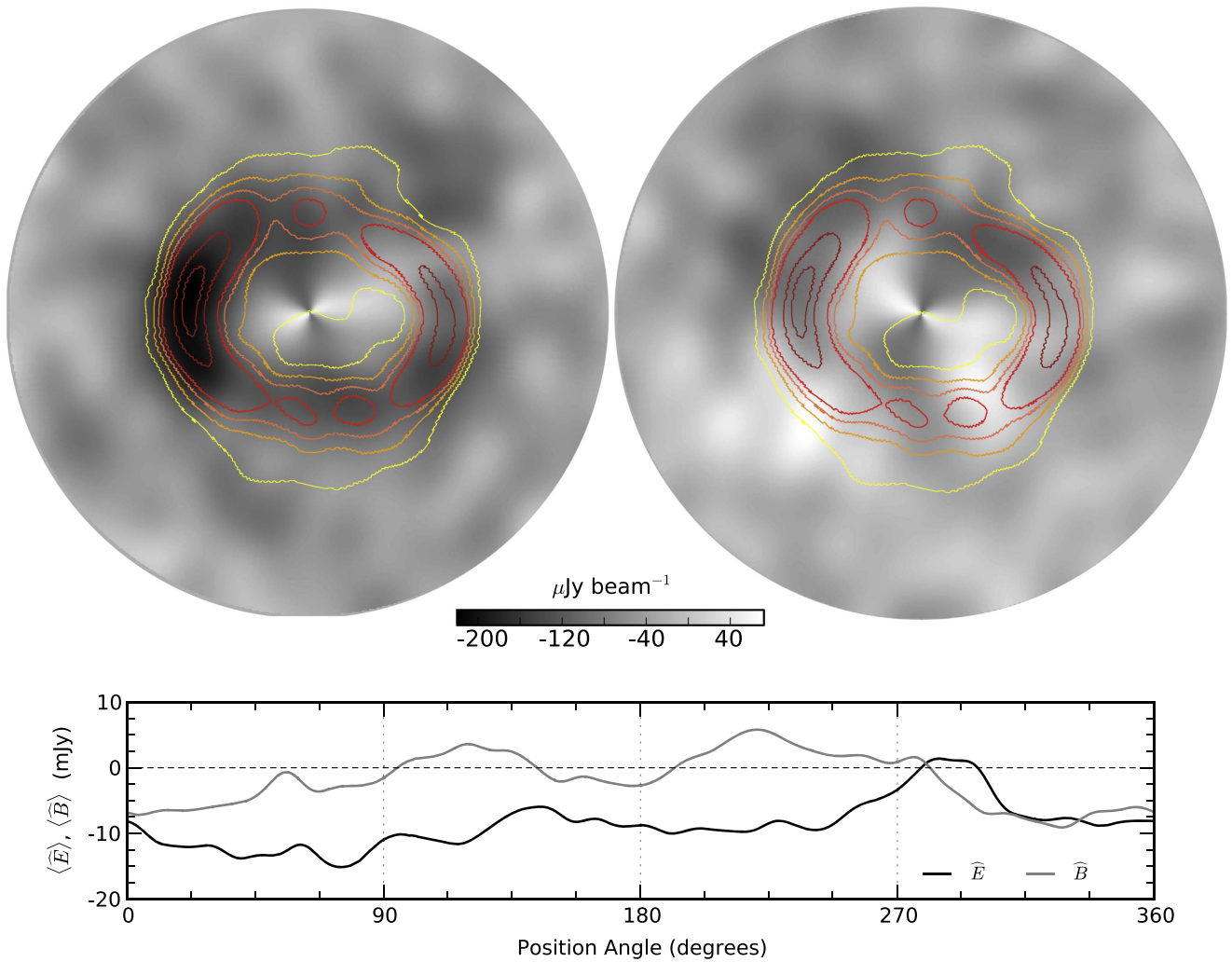


Figure 4. Maps of the \hat{E} (left) and \hat{B} (right) polarizations generated for observations of SNR 1987A at 22 GHz. From the linear polarization Stokes parameters Q and U , $\hat{E} = U \sin(2\chi) + Q \cos(2\chi)$ and $\hat{B} = U \cos(2\chi) - Q \sin(2\chi)$, where χ is the position angle measured from north to east. The map derivation in polar coordinates is centered on the SN site [R.A. $05^{\text{h}} 35^{\text{m}} 27^{\text{s}}.968$, Decl. $-69^{\circ} 16' 11''.09$ (J2000)] (Reynolds et al. 1995), and has a $2''$ radius. In this coordinate system, a negative \hat{E} is equivalent to a tangential polarization vector and therefore to the radial component of the magnetic field, B_{\parallel} , i.e., parallel to the normal of the shock-front plane, while weaker non-radial field components can be traced by the negative \hat{B} . Both maps are superimposed with the contours of the Stokes- I intensity map at 44 GHz, which has a resolution of $0''.2$ (FWHM). The contours are shown at 14%, 22%, 30%, 38%, 70%, and 90% flux density levels, with a color scheme from yellow to brown to identify regions of increasing brightness. The integrated intensity of the \hat{E}/\hat{B} parameters for each subtended angle (north to east, with north at $\text{PA} \equiv 0^{\circ}$ and east at $\text{PA} \equiv 90^{\circ}$) is shown in the bottom plot. The \hat{E} polarization intensity is integrated along a $2''$ radius and shown in black, while the integrated intensity of the \hat{B} polarization is plotted in gray.

such Mach numbers, strong fluctuations in B -field strength would invoke nonlinear cosmic-ray-excited turbulence (Bell 2004).

The relative ratio of the coherent and disordered magnetic field components can be assessed via inspection of the degree of polarization of the synchrotron emission. As introduced in Section 3.2, we use $\hat{E}-I$ plots to determine the fractional polarization in the SNR. The $\hat{E}-I$ plots derived for observations at 22 and 44 GHz (Figure 5) show that the degree of polarization is mostly constant across the remnant. From linear fitting of the $\hat{E}-I$ distribution (dashed blue lines in Figure 5), the overall degree of polarization is $1.5\% \pm 0.2\%$ at 22 GHz and $2.4\% \pm 0.7\%$ at 44 GHz. The mean fraction of polarized emission in the brightest sites on the eastern lobe is $2.7\% \pm 0.3\%$ at 22 GHz and $3.5\% \pm 0.7\%$ at 44 GHz. For comparison, observations of Cassiopeia A (Cas A, SN ~ 1680) at 19 GHz yielded 4.5% of linear polarization around the rim and the absence of polarized emission in the center (Mayer & Hollinger 1968). Analysis of the P distribution against the total intensity in Cas A has not revealed

any significant correlation (Anderson et al. 1995), while sites of very faint synchrotron emission in the remnant of SN 1006 have been associated with P values close to the theoretical maximum (Reynoso et al. 2013). The $\hat{E}-I$ plots hint at an increased fraction of polarized emission in the high-emissivity sites of SNR 1987A. This trend is more marked in the higher signal-to-noise observations at 22 GHz, where the fractional polarization appears to increase super-linearly as the emission becomes brighter, and for $I \gtrsim 6.5 \text{ mJy beam}^{-1}$ the $\hat{E}-I$ distribution is better described by a quadratic fit (green line in Figure 5). While a relatively low degree of polarization is not an unequivocal indicator of the extent of the ordered component of the magnetic field, a direct correlation between increasing fractional polarization and brighter emission sites would require high efficiency rates of cosmic-ray production, possibly achieved by short-scale turbulent amplification of the magnetic field interacting with the dense clumps of the CSM (Meinecke et al. 2014). We note that the beam depolarization associated with our observations hampers

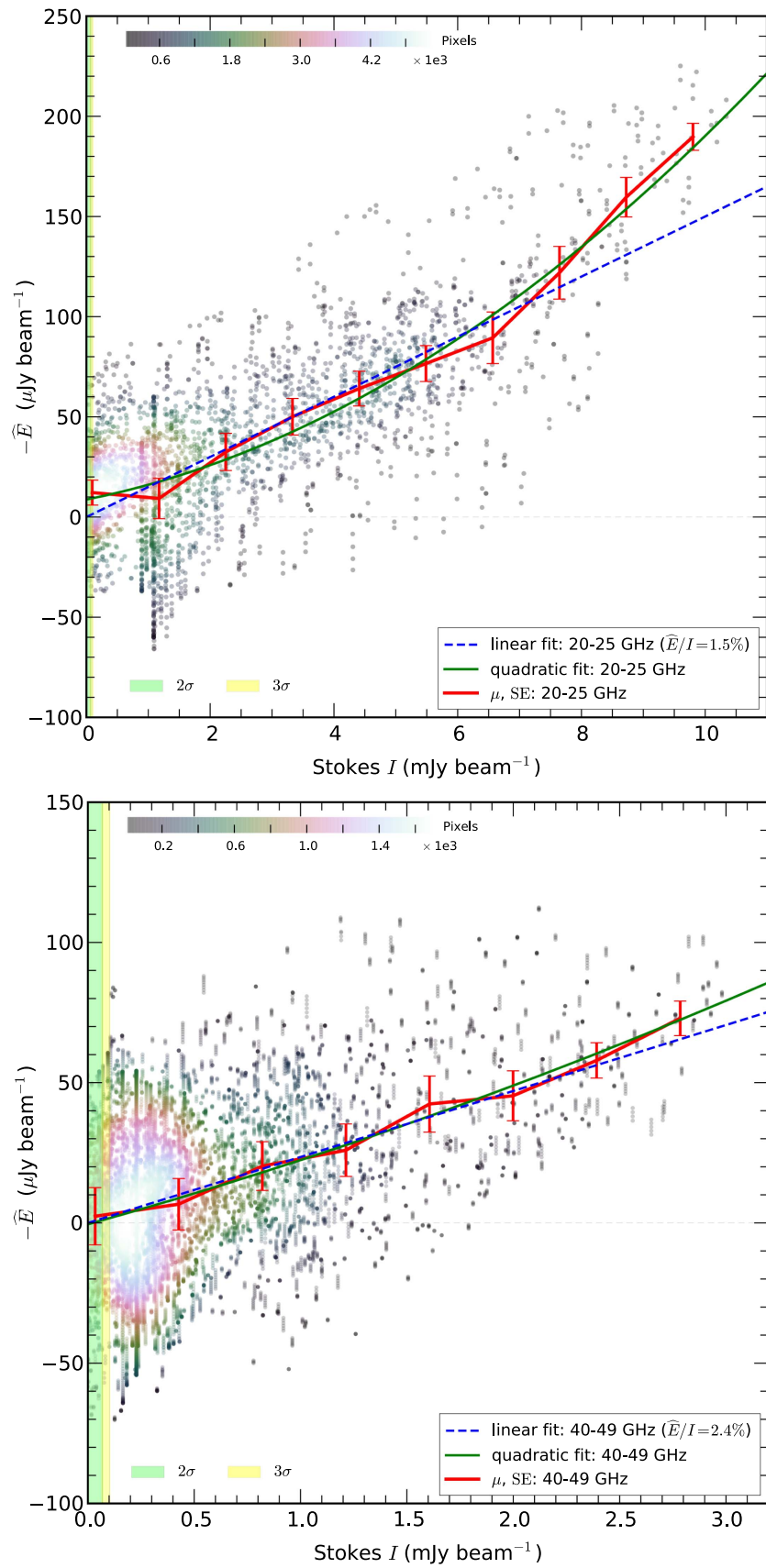


Figure 5. Polarized vs. unpolarized intensities at 22 GHz (top) and 44 GHz (bottom) via \hat{E} - I plots. The Stokes- I and \hat{E} images at 22 and 44 GHz are binned in $0''.1 \times 0''.1$ pixels, with density distribution as shown in the colorbar in the top-left corner. Because the angular resolution (FWHM) of the images is $0''.4$ at 22 GHz and $0''.2$ at 44 GHz, the image pixels have been sampled to limit the correlation within the restoring beam. The \hat{E} - I data have been further binned to derive the mean (μ) and the standard error (SE). The light green and yellow rectangular regions highlight the 2σ and 3σ thresholds of the Stokes- I image. Linear and quadratic fits are plotted with dashed blue and green lines, respectively.

an accurate estimate of the local degree of polarization, especially if the magnetic field undergoes micro-instabilities by the shock front and the downstream regions (Marcowith et al. 2016).


As regards the central region of SNR 1987A, from the distribution of the \hat{E} and \hat{B} polarizations shown in Figure 4, at 22 GHz the inner magnetic field appears to have a prevalence of non-radial components along the northwest–southeast axis, which extend to the outer edge of the ring. The derivation of $P = P(Q, U, I)$ for the inner remnant yields $P = 3.6\% \pm 1.5\%$ at 22 GHz. Although the detection of polarized emission flags the presence of magnetized shocks in the center of the remnant, the 2σ detection cannot be used for a meaningful estimate of the fractional polarization, as the beam depolarization is rather significant for the expected size of a possible pulsar wind nebula (Zanardo et al. 2014).

G.Z. acknowledges the support of the International Centre for Radio Astronomy Research (ICRAR). The ATCA is part of the Australia Telescope National Facility, which is funded by the Australian Government for operation as a National Facility managed by CSIRO.

ORCID iDs

Giovanna Zanardo  <https://orcid.org/0000-0003-2742-771X>

Lister Staveley-Smith  <https://orcid.org/0000-0002-8057-0294>

B. M. Gaensler  <https://orcid.org/0000-0002-3382-9558>

Remy Indebetouw  <https://orcid.org/0000-0002-4663-6827>

C.-Y. Ng  <https://orcid.org/0000-0002-5847-2612>

A. K. Tzioumis  <https://orcid.org/0000-0002-5294-1924>

References

- Abdo, A. A., Ackermann, M., Ajello, M., et al. 2010, *ApJL*, 710, L92
 Ackermann, M., Ajello, M., Allafort, A., et al. 2013, *Sci*, 339, 807
 Anderson, M. C., Keohane, J. W., & Rudnick, L. 1995, *ApJ*, 441, 300
 Arbutina, B., Urošević, D., Andjelić, et al. 2012, *ApJ*, 746, 79

- Badjin, D. A., Glazyrin, S. I., Manukovskiy, K. V., & Blinnikov, S. I. 2016, *MNRAS*, 459, 2188
 Bandiera, R., & Petruk, O. 2016, *MNRAS*, 459, 178
 Beck, R., & Krause, M. 2005, *AN*, 326, 414
 Bell, A. R. 2004, *MNRAS*, 353, 558
 Bell, A. R., & Lucek, S. G. 2001, *MNRAS*, 321, 433
 Blondin, J. M., & Ellison, D. C. 2001, *ApJ*, 560, 244
 Briggs, D. S. 1995, *AAS*, 187, 112.02
 Burn, B. J. 1966, *MNRAS*, 133, 67
 Callingham, J. R., Gaensler, B. M., Zanardo, G., et al. 2016, *MNRAS*, 462, 290
 Drury, L. O’C., & Downes, T. P. 2012, *MNRAS*, 427, 2308
 Drury, L. O’C. 1983, *RPPH*, 46, 973
 Gaensler, B. M., & Bocchino, F. 2012, *SSRv*, 166, 231
 Gull, S. F. 1973, *MNRAS*, 161, 47
 Gull, S. F., & Daniell, G. J. 1978, *Natur*, 272, 686
 Inoue, T., Shimoda, J., Ohira, Y., & Yamazaki, R. 2013, *ApJL*, 772, L20
 Kirk, J. G., Duffy, P., & Gallant, Y. A. 1996, *A&A*, 314, 1010
 Koyama, K., Petre, R., Gotthelf, E. V., et al. 1995, *Natur*, 378, 255
 Marcowith, A., Bret, A., Bykov, A., et al. 2016, *RPPH*, 79, 046901
 Masters, A., Stawarz, L., Fujimoto, M., et al. 2013, *NatPh*, 9, 164
 Mayer, C. H., & Hollinger, J. P. 1968, *ApJ*, 15, 53
 Meinecke, J., Doyle, H. W., Miniati, F., et al. 2014, *NatPh*, 10, 520
 Milne, D. K. 1987, *AuJPh*, 40, 771
 Ng, C.-Y., Gaensler, B. M., Staveley-Smith, L., et al. 2008, *ApJ*, 684, 481
 Ng, C.-Y., Zanardo, G., Potter, T. M., et al. 2013, *ApJ*, 777, 131
 Petruk, O., Orlando, S., Miceli, M., & Bocchino, F. 2017, *A&A*, 605, A110
 Potter, T. M., Staveley-Smith, L., Reville, B., et al. 2014, *ApJ*, 794, 174
 Reynolds, J. E., Jauncey, D. L., Staveley-Smith, L., et al. 1995, *A&A*, 304, 116
 Reynolds, S. P., Gaensler, B. M., & Bocchino, F. 2012, *SSRv*, 166, 231
 Reynolds, S. P., & Gilmore, D. M. 1993, *AJ*, 106, 272
 Reynoso, E. M., Hughes, J. P., & Moffett, D. A. 2013, *AJ*, 145, 104
 Ruzmaikin, A. A., & Sokoloff, D. D. 1979, *A&A*, 78, 1
 Schure, K. M., Vink, J., Achterberg, A., & Keppens, R. 2009, *AdSpR*, 44, 433
 Simmons, J. F. L., & Stewart, B. G. 1985, *A&A*, 142, 100
 Sokoloff, D. D., Bykov, A. A., Shukurov, A., et al. 1998, *MNRAS*, 299, 189
 Zaldarriaga, M., & Seljak, U. 1997, *PhRvD*, 55, 1830
 Zanardo, G., Staveley-Smith, L., Indebetouw, R., et al. 2014, *ApJ*, 796, 82
 Zanardo, G., Staveley-Smith, L., Ng, C.-Y., et al. 2013, *ApJ*, 767, 98
 Zanardo, G., Staveley-Smith, L., Ng, C.-Y., et al. 2017, in Proc. IAU Symp. 331, Supernova 1987A: 30 Years Later—Cosmic Rays and Nuclei from Supernovae and Their Aftermaths, ed. M. Renaud et al. (Cambridge: Cambridge Univ. Press), 274